INTEGRAL

Science Operations Centre

Announcement of Opportunity for Observing Proposals (AO-6)

IBIS Observer's Manual

INT/OAG/08-0298/Dc

Issue 1.0

10 March 2008

Prepared G. Bélanger

Authorised by A.N. Parmar

Based upon inputs from:

P. Ubertini, IBIS Co-P.I., IASF-INAF, Rome

F. Lebrun, IBIS Co-P.I., CEA, Saclay

A. Bazzano, IASF-INAF, Rome

L. Natalucci, IASF-INAF, Rome

J. Lockley, University of Southampton

L. Foschini, IASF-INAF, Bologna

L. Bassani, IASF-INAF, Bologna

V. Bianchin, IASF-INAF, Bologna

D. Götz, CEA, Saclay

P. Barr†, ESA-ESTEC, Noordwijk

E. Kuulkers, ESA-ESAC, Madrid

Table of Contents

1 Introduction

IBIS (**I**mager on **B**oard the **I**NTEGRAL **S**atellite) is one of the two prime instruments of the INTEGRAL scientific payload.

IBIS is a gamma-ray telescope which is able to observe celestial objects of all classes ranging from the most compact galactic systems to extra-galactic objects, with powerful diagnostic capabilities of fine imaging, source identification and spectral sensitivity in both continuum and lines. It covers the entire energy range from about 15 keV to several MeV, and it can localise weak sources at low energies to better than a few arcminutes accuracy. Table 1 gives an overview of the scientific capabilities of IBIS.

Table 1. Overview of scientific capabilities of IBIS

Operating energy range	15 keV - 10 MeV
Continuum sensitivity, in photons $cm^{-2}\ s^{-1}\ keV^{-1}$ (3σ detection, $\Delta E=E/2$, 10^5 s integration) *	2.85×10^{-6} @ 100 keV 1.6×10^{-6} @ 1 MeV
Line sensitivity, in photons $cm^{-2}\ s^{-1}$ (3σ detection, 10^6 s integration)	1.9×10^{-5} @ 100 keV 3.8×10^{-4} @ 1 MeV
Energy resolution (FWHM)	8% @ 100 keV 10% @ 1 MeV
Angular resolution (FWHM)	12'
Point source location accuracy (90% error radius)	30" @ 100 keV (50σ source) 3' @ 100 keV (5σ source) 5-10' @ 1 MeV (5σ source)
Timing accuracy	61 μs - 1 hr
Field of view (FOV)	8.33° × 8.00° (fully coded) 29.11° × 29.42° (zero response)

* The continuum sensitivities are based on in-flight background measurements.

Imaging is performed using coded mask technology. There are two detectors operating simultaneously; the **I**ntegral **S**oft **G**amma-**R**ay **I**mager, ISGRI, a semi-conductor array optimised at lower energies, and the **PI**xellated **C**ea**s**ium **I**odide (**CsI**) **T**elescope, PICsIT, a crystal scintillator for higher energies. The energy ranges covered by ISGRI and PICsIT overlap considerably; ISGRI covers the range 15 keV-1 MeV; PICsIT covers 175 keV-10 MeV. ISGRI is more efficient below about 200 keV (factor ~2 at ~195 keV); PICsIT is more efficient at higher energies (e.g., a factor ~5 at 511 keV) but the different background levels in the two detectors must also be taken into account in the sensitivity calculations (as discussed in Sections 5.3.3). In Figure 1 we show the total effective areas of the two detectors.

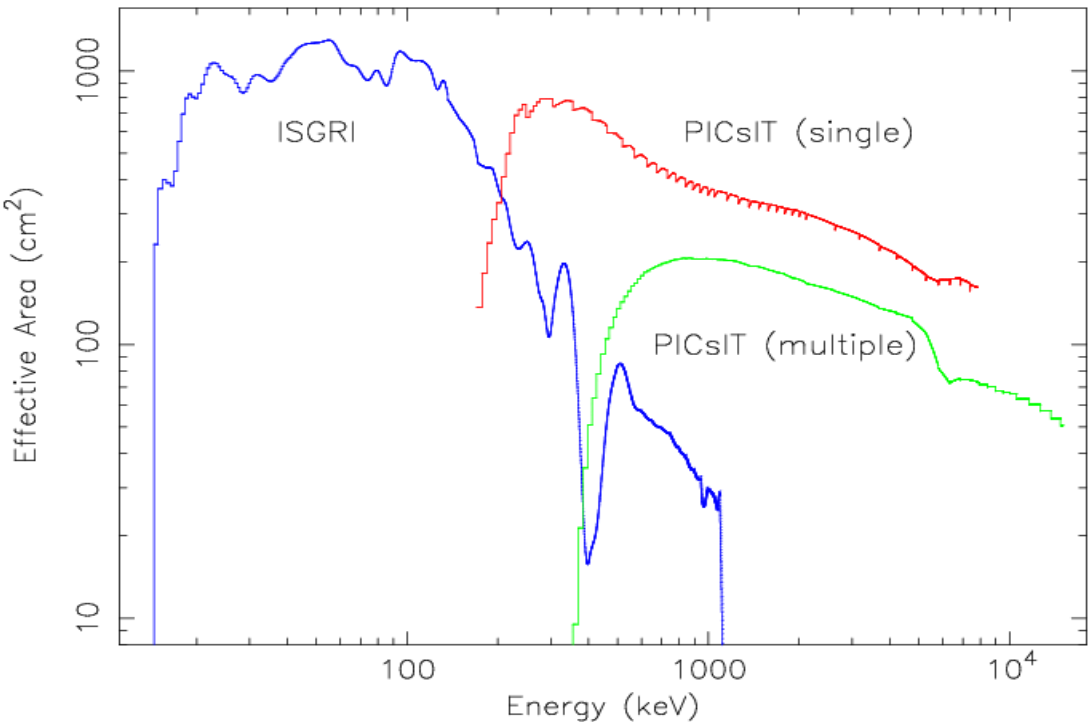

Figure 1: Effective area of the IBIS instruments ISGRI and PICsIT (single and multiple events, see Section 3.1).

Sections 2.1, 5.3 and 6 of this document give the prospective observer a top-level description about the overall design and scientific capabilities of IBIS, to assist in the writing of observing proposals; we recommend these to be studied first. The rest of Section 2 contains a more detailed engineering description of the instrument.

Section 1 gives information about how IBIS actually works, while Section 4 describes the scientific mode of the instrument. Finally, Sections 5.1 and 5.2 describe the in-orbit performance of IBIS and how it is calibrated.

For more details we refer the interested reader to a sequence of papers on the IBIS payload in the A&A special INTEGRAL issue (2003, Vol. 411, L131-L229). This issue also contains various other papers on the first results from in-flight observations.

For descriptions of the IBIS data analysis we refer to, e.g., Goldwurm et al. (2003, A&A 411, L223) and Gros et al. (2003, A&A 141, L179). The validation reports of the ISDC **O**ff-line **S**cientific **A**nalysis (OSA) software package released by the ISDC for ISGRI and PICsIT, as well as descriptions of the data analysis pipelines and modules and the use of the OSA software (see the document "IBIS Analysis User Manual") can be found at the ISDC website (**http://isdc.unige.ch/?Support+documents**).

2 Description of the instrument

2.1 Overall design

IBIS is a gamma-ray imager operating in the energy range 15 keV to 10 MeV, with two simultaneously operating detectors covering the full energy range, located behind a Tungsten mask which provides the encoding and through which the flux is modulated.

The coded mask is optimised for high angular resolution. As diffraction is negligible at gamma-ray wavelengths, the angular resolution of a coded-mask telescope is limited by the spatial resolution of the detector array. The angular resolution of a coded mask telescope is defined by the ratio between the mask element size (in this case 11.2 mm) and the mask-to-detection plane distance (in this case 3.2 m). The IBIS detectors are made of a large number of small, fully independent detection units (pixels).

The detector features two layers, ISGRI (Lebrun et al., 2003, A&A, 411, L141) and PICsIT (Di Cocco et al., 2003, A&A, 411, L189): the first is made of Cadmium-Telluride (CdTe) solid-state detectors and the second of Caesium-Iodide (CsI) scintillator crystals. This configuration ensures a good broad line and continuum sensitivity over the wide spectral range covered by IBIS. The double-layer discrete-element design of IBIS allows the paths of interacting photons to be tracked in 3D if the event is detected in both ISGRI and PICsIT and if the event triggers both ISGRI and PICsIT within 1.9 μs. The application of Compton reconstruction algorithms to these types of events (between a few hundred keV and a few MeV) allows in principle an increase in signal to noise ratio attainable by rejecting those events unlikely to correspond to source photons outside the field of view.

The detector aperture is restricted, in the hard X-ray part of the spectrum, by passive shielding covering the distance between mask and detector plane. An active Bismuth Germanate Oxide (BGO) scintillator Veto system shields the detector bottom as well as the four sides up to the bottom of ISGRI.

Figure *2* shows a cut-away drawing of IBIS (except the mask and the tube).

2.2 Imaging system

2.2.1 The collimator

In order to maintain the low-energy response of IBIS when dithering (see the document *Mission Overview, Policies and Procedures*), the collimation baseline consists of a passive lateral shield that limits the solid angle (and therefore the cosmic gamma-ray background) viewed directly by the IBIS detector in the full field of view up to a few hundred keV.

The tube collimation system is implemented with three different devices:

1) ***The Hopper***: Four inclined walls starting from the detector unit with a direct interface to the IBIS detector mechanical structure. The inclination of the hopper walls should ideally be such that the area laid out by the bottom of walls matches the mask size, but the true inclination takes into account the presence of the Calibration System and the mechanical constraints. The hopper walls reach 550 mm out from the ISGRI top plane (850 mm from the PLM base) while

the actual height is 530 mm. The shielding effect is obtained with Tungsten foils embedded in the four hopper walls. The hopper walls thickness is 1 mm. The hopper is not physically connected to the payload module structure.

2) ***The Tube***: The Tube is formed of four payload module walls, and shielded with glued lead (Pb) foil. Two of the tube walls (± Z axis) are inclined (by about 3.5° to the vertical) in order to follow as closely as possible the inclined tube shape, whilst the Y-axis walls are vertical. In particular the actual inclination of the Z walls is defined by the interface requirements with the hopper: the Z Tube walls stop at 20 mm in the horizontal plane from each upper edge of the hopper walls (i.e. at 850 mm from the Payload Module, PLM, base).

3) ***The mask side shielding***: Four strips of 1 mm thick Tungsten, provide shielding from the diffuse background in the gaps between the mask edges and the top of the tube walls.

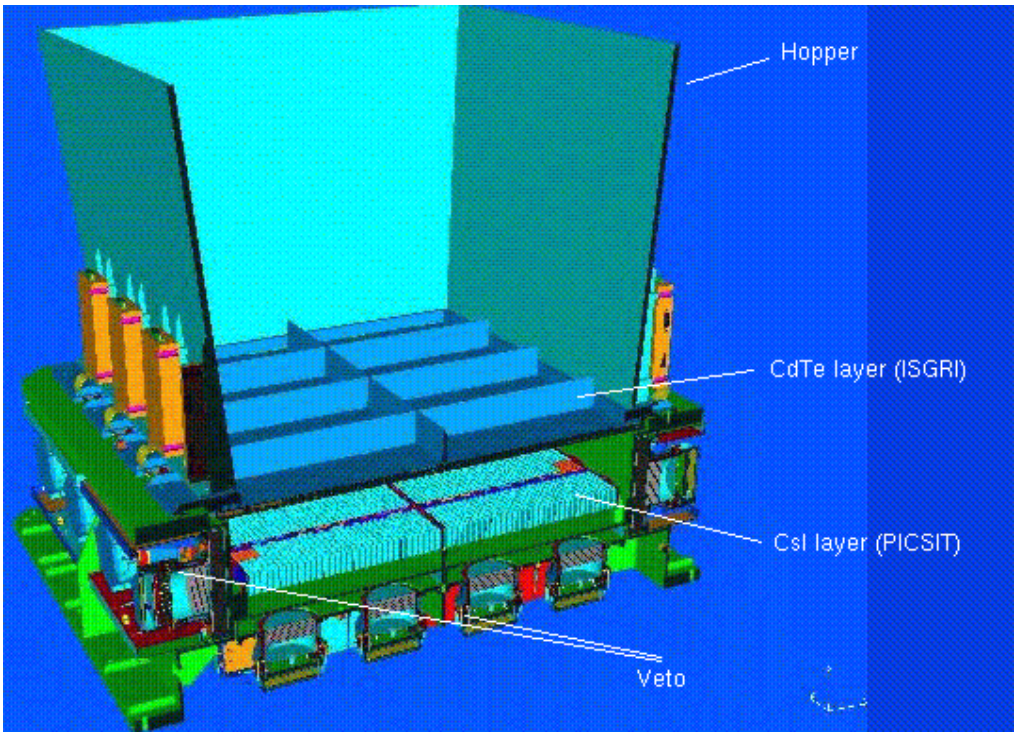

Figure 2. Cutaway drawing of the IBIS detector assembly together with the lower part of the collimator (''Hopper''). The coded mask (not shown) is located 3.2 m above the ISGRI detector.

2.2.2 The mask assembly

The IBIS Mask Assembly is rectangular with external dimensions of 1180 × 1142 × 114 mm^3, and consists of three main subsystems: the Coded Mask, the Support Panel and the Peripheral Frame with the necessary interface provisions.

The Coded Mask is a square of size 1064 × 1064 × 16 mm^3 made up of 95 × 95 individual square cells of size 11.2 × 11.2 mm^2. The cells form a Modified Uniformly Redundant Array (MURA) coded pattern of 53 × 53 elements (see Figure 3. *The IBIS coded mask pattern.*). Approximately half of the cells are opaque to photons in IBIS' operational energy range, offering 70% opacity at 1.5 MeV. The other half of the cells are "open", with an off-axis transparency of 60% at 20 keV.

The Support Panel includes additional elements to support the mask, providing the necessary stiffness and strength to withstand the launch and the in-orbit operational temperatures.

The Peripheral Frame reinforces the sandwich panel and provides the mechanical interfaces with the INTEGRAL PLM.

2.3 Detector assembly

The ISGRI and PICsIT detectors, both of which are situated "under" the coded mask, are separated by 9 cm. PICsIT is situated below ISGRI.

2.3.1 Upper detector layer: ISGRI

Cadmium Telluride (CdTe) is a II-VI semi-conductor operating at an ambient temperature; 0° +/- 20° C is the optimum range. As CdTe detectors can be made to have a relatively small surface, they are ideally suited to build a pixellated imager with good spatial resolution. On the other hand, their small thickness (necessary to achieve good energy resolution) restricts their use to the low energy domain (50% efficiency at 150 keV). Providing spectral performances intermediate between those attained by the cooled Germanium spectrometers (SPI) and the scintillators (PICsIT), CdTe can be well used in the low energy domain (down to ~15 keV).

The CdTe layer is made of 8 identical Modular Detection Units (MDUs) each having 2048 pixels (see Figure 4) which are read out by 512 Application Specific Integrated Circuits, ASICs (4 channels per ASIC). Each MDU is connected independently to a Detector Bias Box (DBB) and to a Module Control Electronics (MCE) system which ensures the A/D conversion and provides other on-board processing such as event filtering and active pixel monitoring.

The specifications of the ISGRI layer are:

- Pixel (CdTe crystal) dimension: 4 x 4 mm^2, 2 mm thick
- Spacing between pixels: 600 μm (4.6 mm centre-to-centre)
- Minimum assembly: polycell of 16 pixels (4 x 4)
- MDU: 128 polycells (16 x 8)
- Layer: 8 MDUs (total of 8 x 64 x 32 pixels)
- Total sensitive area: 2621 cm^2 (16384 x 16 mm^2).

The CdTe layer is located at 294 mm above the PLM base plane and its overall thickness is about 15 mm.

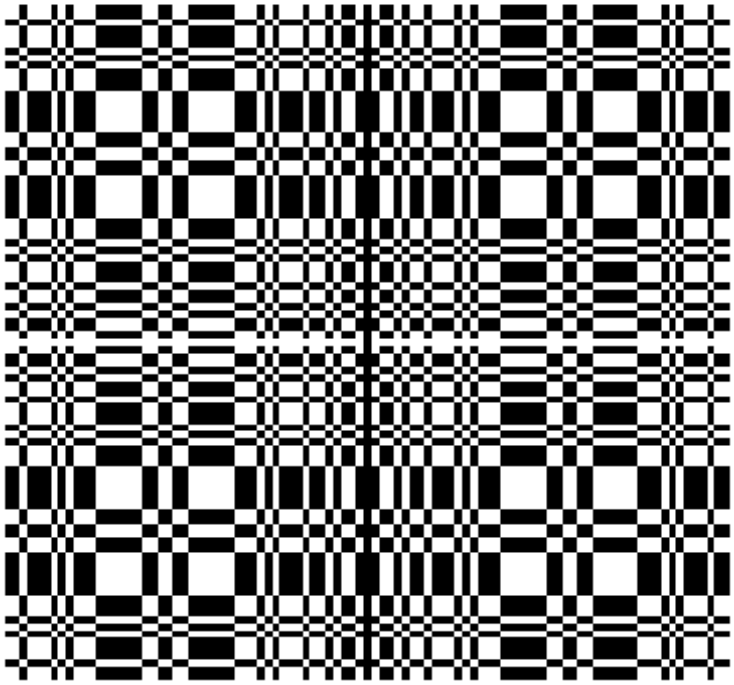

Figure 3. The IBIS coded mask pattern.

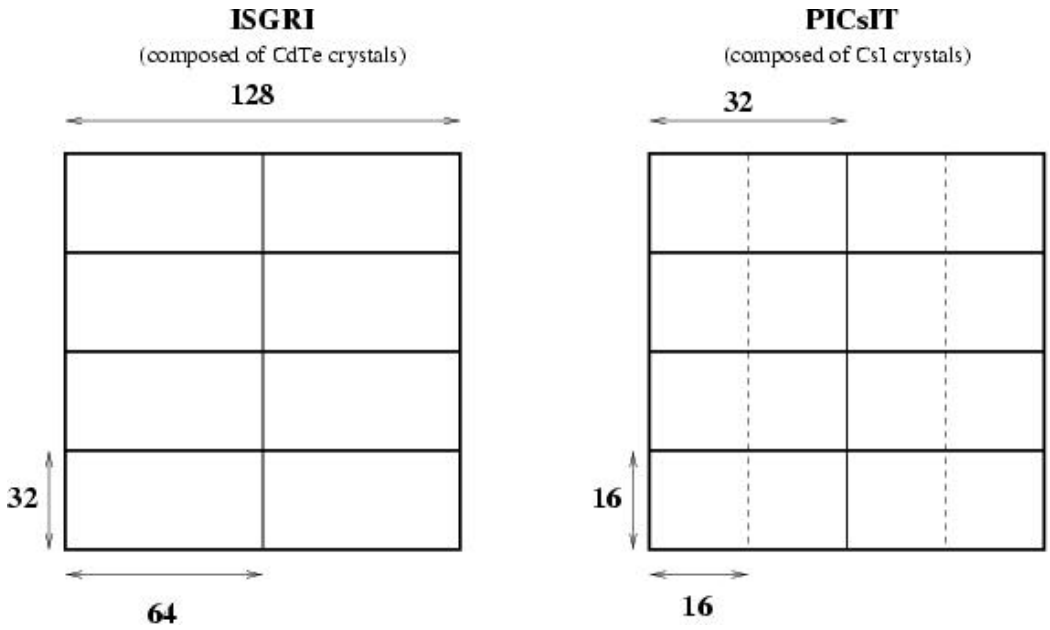

Figure 4: ISGRI (left) and PICsIT (right) detectors division in modules and submodules.

2.3.2 Lower detector layer: PICsIT

Caesium Iodide (CsI) is a I-VII scintillation crystal. The main characteristics of the layer are:

- Pixel (CsI) crystal dimension: 8.55 × 8.55 mm^2, 30 mm thick
- Spacing between pixels: 550 μm (9.2 mm centre-to-centre)
- Minimum assembly (ASIC): 16 pixels (4 × 4)
- Module: 32 ASICs
- Layer: 8 Modules (total of 8 × 32 × 16 pixels)
- Total sensitive area: 2994 cm^2 (4096 × 73.1 mm^2).

The CsI(Tl) bars are optically bonded to custom-made low-leakage silicon PIN photodiodes. The design provides a high degree of modularity. The CsI(Tl) layer is divided in 8 rectangular modules of 512 detector elements, each module being integrated into a stand-alone testable sub-system (see Figure 4). The CsI modules have the same cross-sectional shape as those of the CdTe.

2.4 Veto shield

The Veto shield is crucial to the operation of IBIS, because it is used as part of the anti-coincidence system to discriminate against background particles and photons propagating through or induced within the spacecraft.

The sides, up to the ISGRI bottom level, and rear of the stack of detector planes are surrounded by an active BGO Veto shield. Like the detector array, the Veto shield is modular in construction.

There are 8 lateral shields, i.e., 2 modules per side, and 8 bottom modules.

Each Veto Detector Module (VDM) includes:

- the BGO crystal and related housing
- two photomultiplier tubes (PMTs) optically coupled to the BGO and assembled with the dedicated Front End Amplifiers and High Voltage (HV) divider
- one HV Power Supply
- one Veto Module Electronics box for Module control
- internal harness.

The high density and mean Z of the BGO ensure that a thickness of 20 mm is sufficient to significantly reduce the detector background (caused by leakage through the shielding of cosmic diffuse and spacecraft induced gamma–rays), to less than the sum of all other background components.

2.5 Electronics

2.5.1 Analog Front End Electronics (AFEE)

Charge collection, signal filtering and amplification are all performed by the Application Specific Integrated Circuits (ASICs) on both ISGRI and PICsIT. In ISGRI, the 16384 individual

detector units (pixels) are grouped into *polycells*. A polycell, the basic assembly unit of a detector module, is a hybrid circuit, which receives a signal from 16 detectors via 4 ASICs.

2.5.2 Module Control Electronics (MCE) and PICsIT Electronic Box (PEB)

The MCE and PEB perform receipt, checking and execution of telecommands for ISGRI and PICsIT, respectively. They also collect and format the housekeeping data and process the analogue and digital data (energy and rise time). An important function of the MCE is to monitor the CdTe noise levels. In-flight, a CdTe detector can become noisy and trigger the relevant MCE too frequently, causing a large dead time with unacceptable loss of photons. Therefore, the MCE monitors, in real time, the relative counting rates of each CdTe polycell. If a polycell exhibits noise, the MCE will, if necessary, switch it off (i.e., the pixel becomes "disabled" or "dead"). It can subsequently be reactivated and checked from the ground.

2.5.3 On-board calibration unit

IBIS contains an on-board collimated radioactive ^{22}Na source. This allows regular calibration of PICsIT at both the 511 keV and 1275 keV lines (calibration to better than about 1% in 1–2 orbits). ISGRI can also use the 511 keV line, albeit at lower efficiency.

2.5.4 Digital Front End Electronics (DFEE) and "FIFO"

The DFEE is situated behind the AFEE and processes the ASICs output for the 'first-in, first-out' (FIFO) data manager. FIFO sorts the events from different modules according to their true arrival time in the detector plane for transmission to the DPE/HEPI (see below). The DFEE also monitors the FIFO and instructs it when to send data to the DPE.

2.5.5 Data Processing Electronics (DPE) and Hardware Event Processor (HEPI)

The detector electronics chain ends at the DPE and the HEPI. The HEPI performs the data histogramming and generates the data structures for the DPE. The DPE handles all the interfaces between the instruments and the spacecraft for both uplink and downlink. For example, it handles the packetting of data for the On-Board Data-Handling System before transmission to the ground.

3 How the instrument works

3.1 Detection

Photons are detected in IBIS by several methods:

Detection in ISGRI: a photon is stopped in a single pixel of the semi-conductor, generating an electric pulse.

Detection in PICsIT: a photon passes through ISGRI and is stopped in PICsIT, generating one or more scintillation flashes. PICsIT records detections which occur in just one pixel (single events), and detections which occur in more than one pixel (multiple events), separately.

Detection in both ISGRI and PICSIT (Compton mode): Photons arriving in either ISGRI or PICsIT may undergo a Compton scattering and be subsequently detected in the other layer. Analysis of Compton events will likely be supported in the next release of the OSA software. For the moment, these events are not taken into account in the sensitivity calculations.

In Figure 5 shown below we show the estimated efficiencies of the various detection techniques.

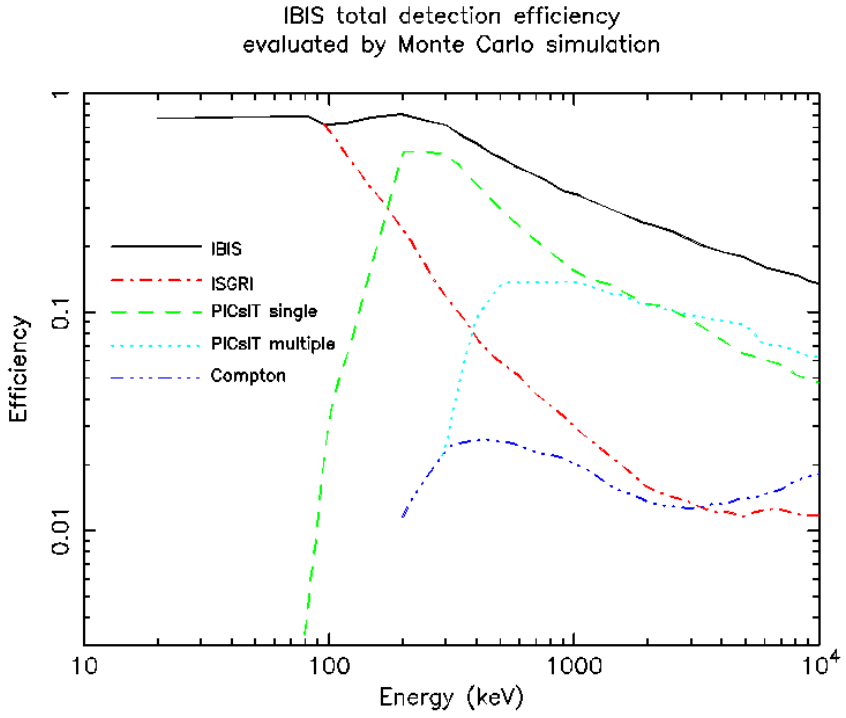

Figure 5. IBIS efficiency for the different detection techniques.

3.2 Imaging

Both ISGRI and PICsIT record the (x,y) coordinates of each event registered in the corresponding layer to construct a shadowgram (a detector-plane image of the coded-mask shadow). The anti-coincidence VETO is used to reject background events.

A photon detected in one pixel of a detection layer may be due to the background or to any celestial source visible from this pixel through the holes of the mask. It is therefore not possible to assign a given photon to a given source. On the other hand, cross-correlation techniques applied to a statistically significant ensemble of photons allow for a full reconstruction of the sources located in the Fully Coded Field Of View (FCFOV: 8.3° x 8.6°). For the Partially Coded Field of View (PCFOV: out to 30.6° x 31°), special cleaning techniques must be applied to the data for a proper image reconstruction.

The actual sky coverage during an observation depends on the dither pattern. For example, during a 5x5 dither pattern a 36.3° x 36° field is imaged out to zero response, while a 16.3° x 16° region is sampled (at least partly) with full coding.

3.3 Spectroscopy

3.3.1 Detection in ISGRI

In principle, the amplitude of the pulse yields the energy of the incident photon. However, above 50 keV the energy determined is a function of the pulse height and rise time, so both must be used to determine the energy of the incident photon. In addition, the resulting line profile (energy resolution) is no longer Gaussian, but more similar to a Lorentzian. The energy resolution depends on the operating temperature and also on the bias voltage; the bias voltage has to be optimised as a trade-off between high resolution but more noise (high voltage) or lower noise but lower resolution (low voltage).

3.3.2 Detection in PICsIT

The energy of the incident photon is derived, in each crystal bar, from the intensity of the flash recorded in the photodiode. For multiple events it is derived by summing the energies derived from the intensity of each of the flashes. The energy resolution of PICsIT is a function of the signal-to-noise ratio of the events, the electronic noise at low energies and the light output.

3.3.3 Compton events

For Compton events the energy is determined from the sum of energies for the initial event and the scattered photon. Note again that the analysis of Compton events is currently not supported.

3.4 Timing

The ISGRI time resolution is 61.035 μs for each detected event. PICsIT spectra and images are accumulated every 1800-3600 seconds depending on the (flexible) dithering time; a spectrum alone (but with low resolution, from two to eight energy bands) is available every several ms1. See §5.3.5 for further details.

3.5 Polarimetry

In principle, the multiple events in adjacent PICsIT cells can be used to determine the polarisation of the incident photons, because of the Klein-Nishina cross-section dependence with polarisation angle. However, at present polarisation studies are not feasible, and it is, therefore, not offered in this AO.

4 Overview of observing modes and parameters

IBIS has several observing modes for engineering and calibration purposes. However, for scientific use there is only one operating mode: Science Mode. This mode has no user-selectable parameters.

In Science Mode, ISGRI registers and transmits events on a photon-by-photon basis, i.e. every event is tagged with its (x,y) position on the detector plane, energy (from the pulse height and rise time) and event time.

PICsIT, in principle, can also operate in photon-by-photon mode. However, given the higher background compared to ISGRI, with the available telemetry there would be unacceptable data losses. Therefore, the standard mode for PICsIT is *histogram*. Images and spectra (full spatial resolution, 256 energy channels) are accumulated for 1800-3600 seconds (depending on the flexible dithering time) before transmission to ground. There is no time-tagging internal to the histogram, i.e., spectral imaging has a time resolution of 1800-3600 seconds only.

In addition, coarse spectra without imaging information are accumulated by PICsIT and transmitted with far higher time resolution. However, without imaging information, their usefulness is limited to observations of very strong sources where the source count rate dominates the background. The time resolution and the number of energy channels for this spectral timing data can be set from the ground. The time resolution can take values between 0.976 ms to 500 ms. Currently used values are 15.625 ms and 8 energy channels (i.e., 208-260 keV, 260-312 keV, 312-364 keV, 364-468 keV, 468-572 keV, 572-780 keV, 780-1196 keV and 1196-2600 keV). The characteristics of the different observing modes for IBIS are summarized in Table 2.

Table 2: Overview of IBIS observing modes

	Observing Mode	Detector image resolution (pixels)	Timing resolution	Spectral resolution (channels)
ISGRI	photon-by-photon	128x128	61.035 μs	2048
PICsIT	photon-by-photon	64x64	64 μs	1024
	spectral-imaging	64x64	30-60 min	256
	spectral-timing	none	1-500 ms	2-8

5 Performance of the instrument

5.1 Components and sources of instrumental background

For most astronomical sources, the background will be higher than the measured source intensity. The main sources of background in IBIS are:

- for ISGRI at low energies (up to about 100 keV), the fluorescence emission of the passive shield elements and the diffuse cosmic gamma-ray background;
- for ISGRI at higher energies, and for PICsIT, the radioactive decay of unstable nuclei created by the spallation interactions of cosmic-ray protons and their secondary particles in the massive parts of INTEGRAL.

Other effects which influence the background are, e.g., solar activity and VETO performance. The particle background varies over the solar cycle. It is lowest at solar maximum, when the higher solar magnetic field inhibits the propagation of cosmic rays into the inner solar system. It is expected to be a factor of ~2 higher at solar minimum.

The reduction in count rates compared to the no-VETO case has been evaluated during the Performance Verification (PV) phase to be of the order of about 50% for ISGRI and about 40% for PICsIT. The actual Veto configuration has been optimised to give the best uniformity of Veto operation.

Typical in-flight background spectra as observed by ISGRI and PICsIT are shown in Figure 6. In Figure 7, we show the evolution of the total PICsIT count rate as a function of revolution number. The observed background rates compared to the Crab on-axis count rates are given in Table 3. The background rates quoted here are determined in-flight using calibration observations.

The (background) detector images are strongly structured (apart from dead pixels, see next Section). They have been evaluated in order to be taken into account in the background subtraction algorithms. Background maps from large sets (up to ~1.7 Ms) of empty fields or high latitude observations performed in 2003 and 2004 are included by default in OSA. These maps optimize background subtraction and allow to reach higher signal-to-noise in the detections.

Already since the first instrument activation, frequent bursts of counts in the PICsIT count rate have been observed. In the accumulated detector images they are seen as tracks of bright pixels; they indicate that these events are related to the interaction of cosmic rays with the detector. The contribution of these cosmic-ray induced triggers to the total PICsIT background is of the order of 10%. However, these triggers are mainly effective at low energy channels, i.e., below ~300 keV (up to about 30% of the total background). Since in the standard observing mode only histograms are downloaded, this introduces non-statistical fluctuations in the data, up to a factor of a ~2.5 in the signal-to-noise. A study to remove these fake events onboard is ongoing.

IBIS is located next to SPI and JEM-X (see the *Integral Manual*), both also coded-mask telescopes. Since gamma-rays are highly penetrating, it is possible for them to pass through parts of the spacecraft or instrument structures, as well as coded masks, and to be detected by the gamma-ray instruments. Therefore, off-axis gamma-rays (effectively those with energies above ~300 keV) that pass through either the SPI or the JEM-X coded masks may cast a shadow

of this mask onto the IBIS detectors (see Figure). The former combination is often referred to as the ''SPIBIS'' instrument. Although it effectively increases the field of view of IBIS, a bright gamma-ray source would thus add additional counts and modulation to the IBIS histogram, which considerably complicates the image reconstruction.

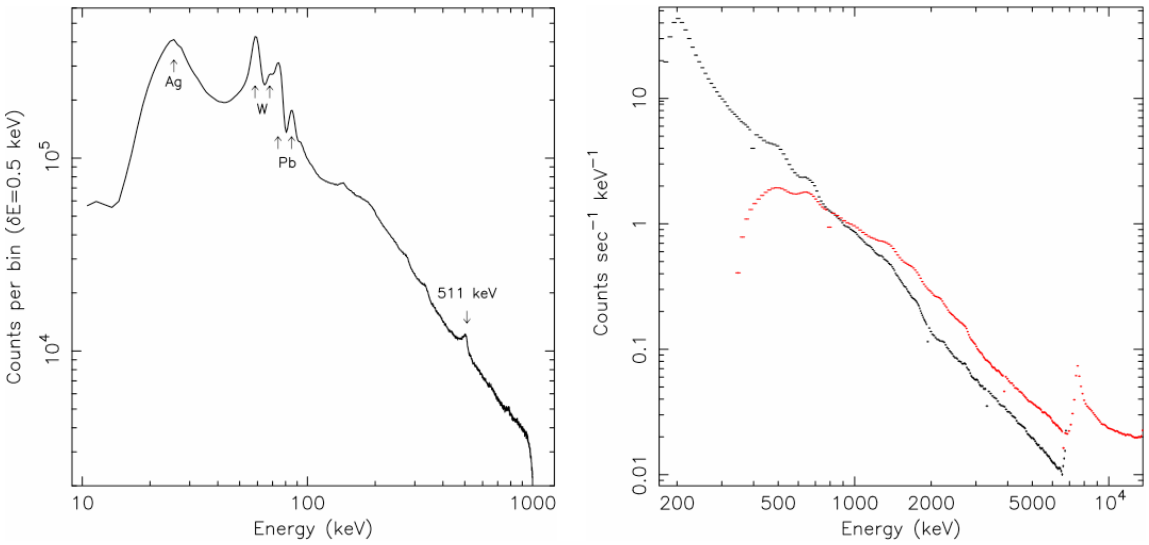

Figure 6. In-orbit background spectra for ISGRI (left) and PICsIT (right) with OSA 7. The ISGRI spectrum is from empty field observations in revolution 96 (effective exposure time 36.4 ks). For PICsIT the single (black) and multiple (red) events contributions to the background are shown separately; based on one Science Window of data accumulated in revolution 500.

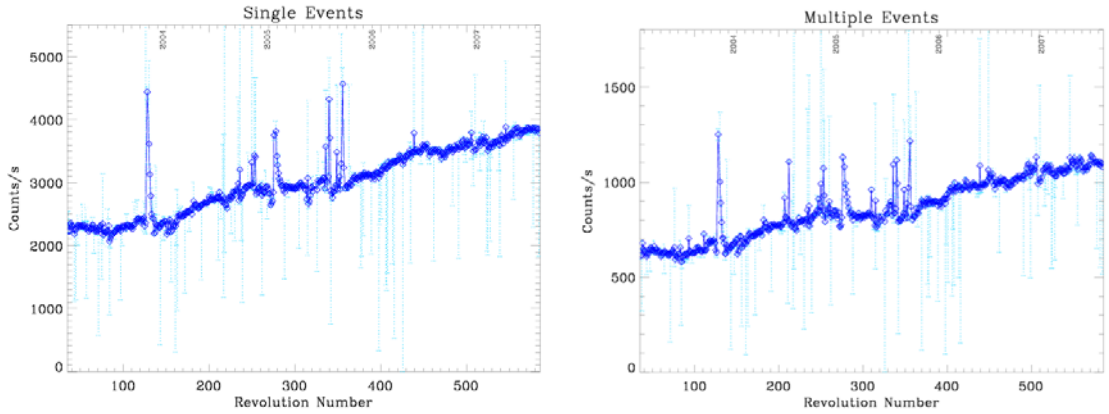

Figure 7. Total PICsIT count rate as a function of time (revolution number), computed with OSA 7 at the science window level. The left panel shows the count rate for all single events and the right panel shows the count rate for multiple events.

Table 3. Background rates compared to the Crab rates (OSA 6)

Energy band	Background (Solar Max) cts s^{-1}	Crab on-axis cts s^{-1}	
ISGRI: 15-400 keV	600	250	
PICsIT:		single	multiple
203-252 keV		2.71±0.02	–
252-336 keV		2.46±0.01	–
336-448 keV		1.17±0.01	0.07±0.01
448-672 keV		0.60±0.01	0.14±0.01
672-1036 keV		0.26±0.01	0.14±0.01
1036-1848 keV		0.06±0.01	0.12±0.01
(203-1036 keV; single)	2500	7.20±0.03	
(336-1848 keV; multiple)	580		0.47±0.02

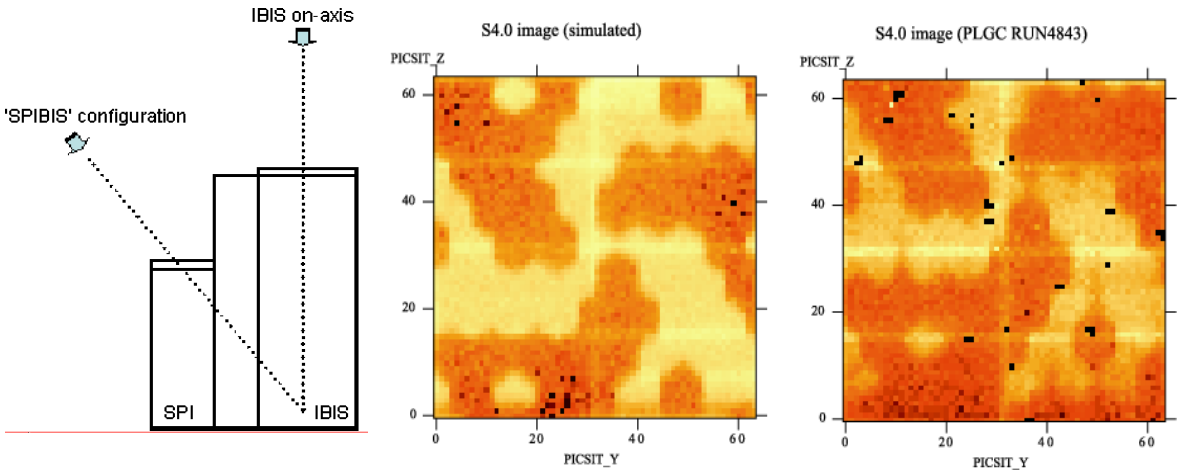

Figure 8. Left: Off-axis source positions for the SPIBIS configuration as well as the shielding tests, during the pre-flight calibrations. Middle and right: PICsIT shadowgrams from simulations (middle) and pre-flight calibration data (right). The images are slightly offset due to the inaccuracy in the supplied source position.

IBIS is located next to SPI and JEM-X, both also coded-mask telescopes. Since gamma-rays are highly penetrating, it is possible for them to pass through parts of the spacecraft or instrument

structures, as well as coded masks, and to be detected by the gamma-ray instruments. Therefore, off-axis gamma-rays (effectively those with energies above ~300 keV) that pass through either the SPI or the JEM-X coded masks may cast a shadow of this mask onto the IBIS detectors (see Figure 8). The former combination is often referred to as the ''SPIBIS'' instrument. Although it effectively increases the field of view of IBIS, a bright gamma-ray source would thus add additional counts and modulation to the IBIS histogram, which considerably complicates the image reconstruction.

The SPIBIS effect has been calibrated before launch. ISOC avoids scheduling sources when either of the three brightest sources/regions, i.e., Crab, Cyg X-1 or the Galactic Center region, are visible by IBIS through the SPI mask. This ensures that the observation is uncontaminated by a possible SPIBIS effect.

5.2 Instrumental characterisation and calibration

The ISGRI and PICsIT detectors were, and still are, calibrated in-orbit. Observations of the Crab nebula and pulsar are performed to enable regular verification of the detector uniformity and its energy response, as well as enhancing the calibration. Also, investigations are still ongoing by using a mass model and Monte Carlo simulations, to further understand the instrument characteristics. At present the calibration is good up to the few % level for ISGRI and about 5% level for PICsIT at off-axis angles less than ~10°. This means that in the spectral fits the deviations between the observed spectrum and actual model are generally within 5%. As an example, Figure 7 displays a Crab calibration spectrum, showing the status of the calibration.

The instrument characteristics are also checked after strong disturbing events such as solar flares. The energy response and spectral resolution are monitored on long time-scales using the de-excitation lines at 511 keV and 1275 keV emitted by the on-board ^{22}Na calibration source, and at 59.3 keV using the background-induced Tungsten fluorescence line from the coded mask and hopper walls.

ISGRI shows a loss of gain of about 3% per year. Additional gain drops (0.6-1%) occurred after (strong) solar flares. The data analysis software therefore contains a time-dependent gain correction for ISGRI. Variations due to global temperature changes (~5°) are taken into account with an accuracy of 0.5%. Taking into account the expected PICsIT gain variation of 0.3% $^{o}C^{-1}$ measured during on-ground thermal tests, the average gain (over the whole detection plane) measured in-flight indicates that the PICsIT temperature gradient along the INTEGRAL orbit is the dominant factor in the observed PICsIT gain variation.

At high energies (typically >1 MeV), the background so strongly dominates the flux of any calibration source that a large amount of data is needed. It was not possible to take sufficient measurements in the few weeks of the commissioning phase. Therefore, data accumulated through routine operations are used to extend the calibration into the MeV region.

The current number of disabled (or 'dead') pixels for ISGRI is stable at ~500 (of a total of 16384 pixels). For PICsIT the current number of disabled pixels is stable at ~52 (of a total of 4096 pixels).

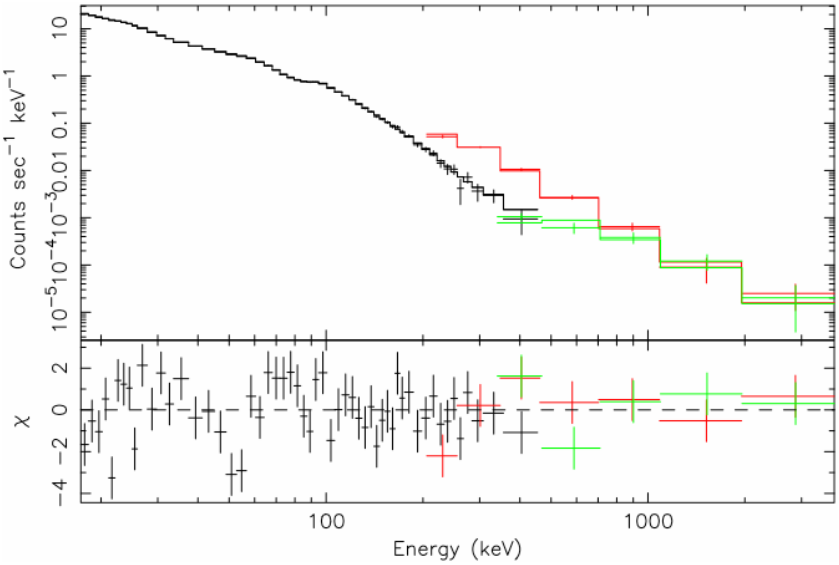

Figure 7. IBIS Crab photon spectrum. The fit to the data is done with a broken power-law model whose best fit parameters are $\Gamma_1 = 2.09^{+0.003}_{-0.015}$, $E_{break} = 96.27$ keV, and $\Gamma_2 = 2.29^{+0.056}_{-0.045}$, with a normalisation at 1 keV of 9.67 photons cm^{-2} s^{-1} keV^{-1}. The ISGRI data (black) was collected during an on-axis staring observation in revolutions 300 (net time of 31 ks), and the PICsIT data was collected in revolutions 39-45 (net time of 563 ks), for single (red) and multiple events (green). The analysis was done with OSA 7.0, and a systematic error of 1% was added to each spectral bin. The reduced is χ^2 =1.73 (χ^2 = 105.8 for 61 degrees of freedom). The intercalibration constant between ISGRI (set as reference) and PICsIT is 0.56±0.04.

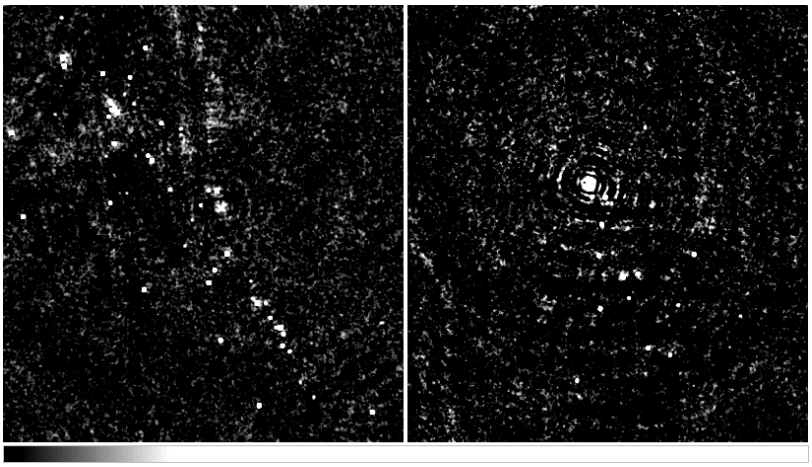

Figure 8. A comparison between two significance mosaics (18-25 keV) of equal exposure (~2 Ms) obtained from observations done with the 5x5 dithering mode (left, Galactic Center field) and the hexagonal dithering mode (right, GRS 1915+105 field). The significance scale runs from 2 to 50σ. OSA software version 5.1 has been used. Clearly, the mosaic derived from hexagonal dither mode observations still suffers from a systematic circular effect on a large spatial scale, despite improvements in the analysis procedures.

5.3 Measured performance

5.3.1 Imaging resolution

In the FCFOV the off-axis response (sensitivity, spatial resolution) is fairly uniform, at least above ~30 keV (at the lowest energies the off-axis transparency of the mask falls off quickly). However, if a 5x5 dither pattern is used, there is a slight (~2%) loss in overall sensitivity averaged over the dither pattern.

The angular resolution of IBIS is 12' FWHM. However, a feature of the mask is that the centroiding accuracy for a point source can be much finer. Figure 9 shows the point source location accuracy (PSLA) in ISGRI as a function of signal-to-noise ratio from observations (points) and theory (line). The absolute localisation (after misalignment correction) is better than 50" for bright sources (>10σ). The PICsIT PSLA is a factor ~2 coarser (see Figure 10).

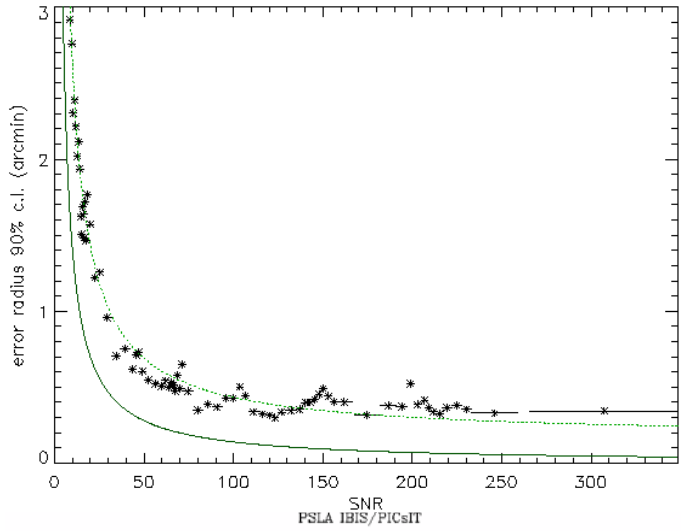

Figure 9. The point source location accuracy (PSLA; 90% confidence level) as a function of the measured source signal-to-noise ratio (SNR) for ISGRI using in-flight calibration observations of Crab, Cyg X-1 and Cyg X-3 in the 20-300 keV band, with source positions ranging between 0° and 14° from the telescope axis. The theoretically expected curve (continuous line) is also shown. The dotted line shows the fit to the data points: Location Error Radius (90%) = 22.1 $(SNR)^{-0.95}$ + 0.16 arcmin.

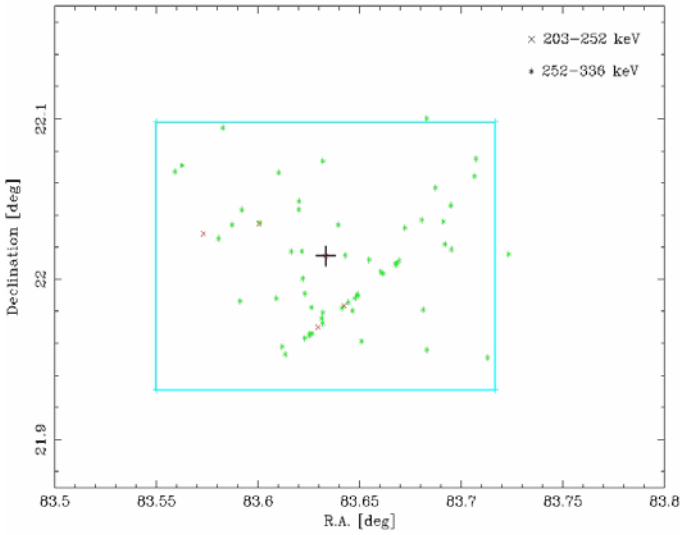

Figure 10. The point source location accuracy (PSLA) for PICsIT using Crab observations from revolutions 39, 43, 44 and 45. Results for 2 energy bands are given (203-252 keV and 252-336 keV). Only detections with at least 3σ per science window (or exposure) are used. The catalog position of the Crab is indicated with a cross at the centre of the plot; the rectangle around it represents the dimension of one pixel of PICsIT (10' size).

Observers should keep in mind that when INTEGRAL is performing staring observations, clear residual systematic structures are seen in the reconstructed sky images that can degrade the science objectives. It is therefore advised to use one of the dithering modes, where the 5x5 dither is preferred (see Figure 8). If a strong source (such as the Crab) is within the field of view but only partially coded, so-called ghosts may appear in the reconstructed sky images. In these cases we recommend to using, if possible, a different pointing so that the contaminating source falls outside the partially coded field of view.

5.3.2 Spectral resolution

The spectral resolution of ISGRI has been measured during pre-flight tests on the engineering model, as well as in-flight (Figure 11). Resolutions of 9% at 60 keV (W fluorescence) and 4.6% at 511 keV have been measured from in-flight spectra. These results are in perfect agreement with the pre-flight measurements and show the stability of the instrument, even after disturbing events such as solar flares. Figure 12 shows the PICsIT spectral resolution, as determined in-flight. The in-flight data show no degradation or changes in the PICsIT spectral performance.

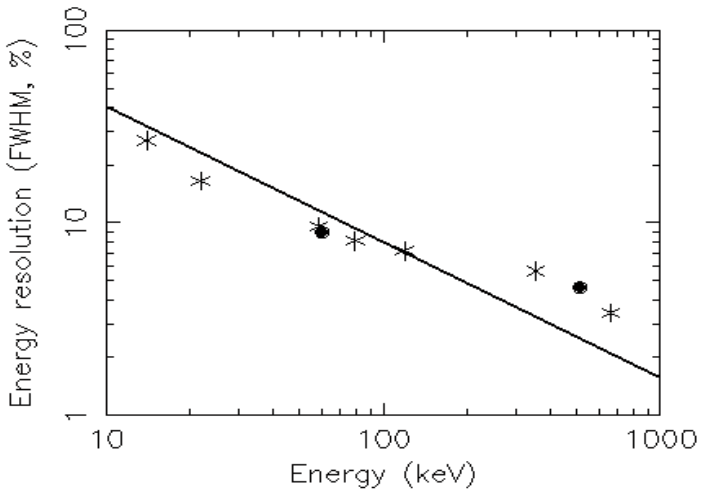

Figure 11. The energy resolution of ISGRI. Solid line: theoretically expected values; points (stars): values measured before launch using an engineering model. The study of the in-flight W fluorescence line at 60 keV and the e^+/e^- annihilation lines at 511 keV (shown as filled circles) do not reveal any evidence of a change of the ISGRI spectral performance.

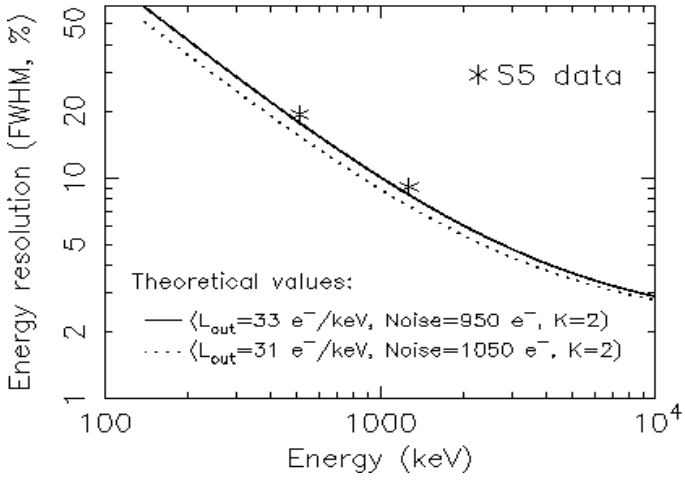

Figure 12. PICsIT energy resolution at 511 and 1275 keV as measured in-flight using Calibration Unit (S5) data (shown as stars). Also shown are the theoretical expectations as determined from pre-flight tests using an engineering model. The electronic-noise values (''Noise'') refer to one ASIC only; a 10% increase is expected when extrapolating to the complete detector electronic chain.

5.3.3 Sensitivity

The full calculations for continuum and line sensitivities are given by the following equations:

Continuum

$$S_c = n_\sigma \, [TA\Delta E \, \varepsilon_T \varepsilon_I \, (\vartheta_o - \vartheta_c)^2]^{-1} \{n_\sigma (\vartheta_o + \vartheta_c)^2 + [n_\sigma 2(\vartheta_o - \vartheta_c)^2 + 4(\vartheta_o - \vartheta_c)^2 \, T\Delta E \, AB]^{0.5}\} \quad \textbf{[Eq. 5.3.3.1]}$$

Line (narrow)

$$S_l = n_\sigma \, [TA\varepsilon_p \varepsilon_I \, (\vartheta_o - \vartheta_c)^2]^{-1} \{n_\sigma (\vartheta_o + \vartheta_c)^2 + [n_\sigma 2(\vartheta_o - \vartheta_c)^2 + 4(\vartheta_o - \vartheta_c)^2 \, T\delta E \, AB]^{0.5}\} \quad \textbf{[Eq. 5.3.3.2]}$$

where:

- S_c is the continuum sensitivity in photons cm^{-2} s^{-1} keV^{-1},
- S_l is the line sensitivity in photons cm^{-2} s^{-1},
- n_σ is the number of sigma,
- ΔE is the energy bin (continuum),
- δE is the energy resolution,
- A is the detector area,
- ε_p, ε_T are the peak and total efficiencies,
- ε_I is the imaging efficiency, a function of the coding noise and dither pattern,
- B is the background count rate in counts cm^{-2} s^{-1} keV^{-1},
- ϑ_o, ϑ_c are the open and closed mask element transparencies, and
- T is the observation duration.

Note that for a broad line with a FWHM of ΔE keV, the sensitivity is reduced by $(\Delta E/\delta E)^{1/2}$.

The ISGRI and PICsIT broadband, statistically limited continuum and line sensitivity curves parametrised in Eqs. 5.3.3.1 and 5.3.3.2 are shown in Figure 13. Tables 4, 5 and 6 give some of the actual values. Note that the PICsIT sensitivities have not changed with respect to AO-3 esitmates. They agree with the observed sensitivities within a factor of ~2. This difference is due to systematics, which increase partly due to long observations (typically >500 ks), and partly due to a large number of source in the range 20–150 keV. The latter does not affect the sensitivity at higher energies where there are few bright sources. As an example, the continuum sensitivities deduced from Crab observations are shown in Figure 16. For reference, the ISGRI sensitivities are also compared in three energy bands in Table 7.

The online Observation Time Estimator (OTE) uses the most recent ISGRI sensitivity curves. In Sections 6.2 and 6.3 we explain how the sensitivities may be used to estimate signal-to-noise ratios and observing times.

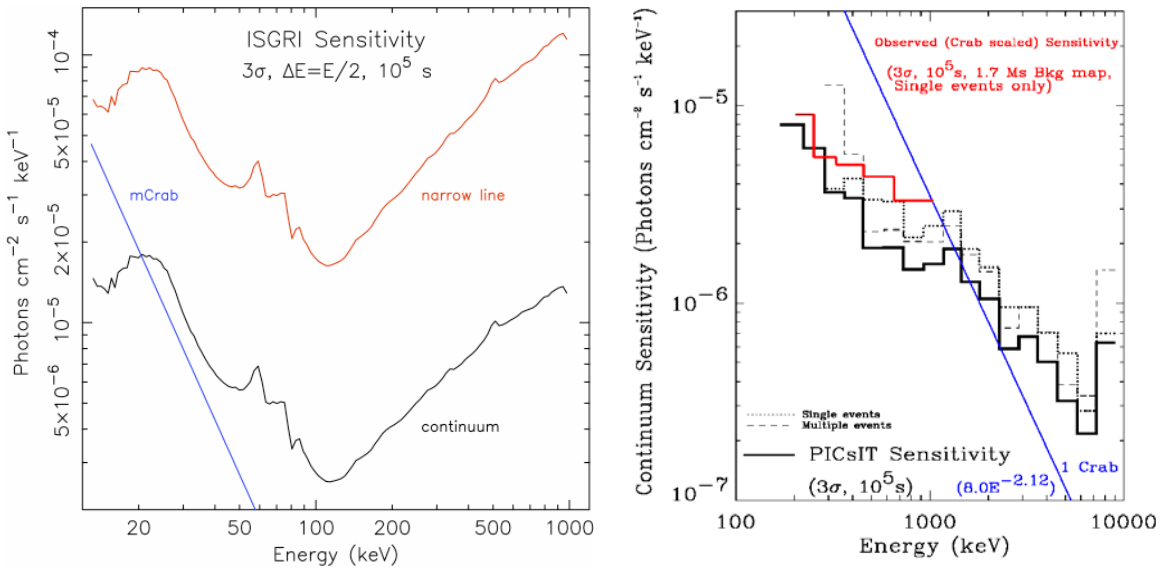

Figure 15. Left: Most recent update to ISGRI continuum (black) and narrow line (red) sensitivity derived from Crab observations processed with OSA 7. Right: PICsIT statistically limited continuum sensitivity is given by the black histograms, from single events (dotted), multiple events (dashed), and combined (solid), all scaled to the in-flight background count rate, and compared with the sensitivity obtained by scaling from the Crab observation using OSA 5 (red; single events only). All sensitivities are for 10^5 s exposure time, 3σ detection and continuum binned to ΔE= E/2.

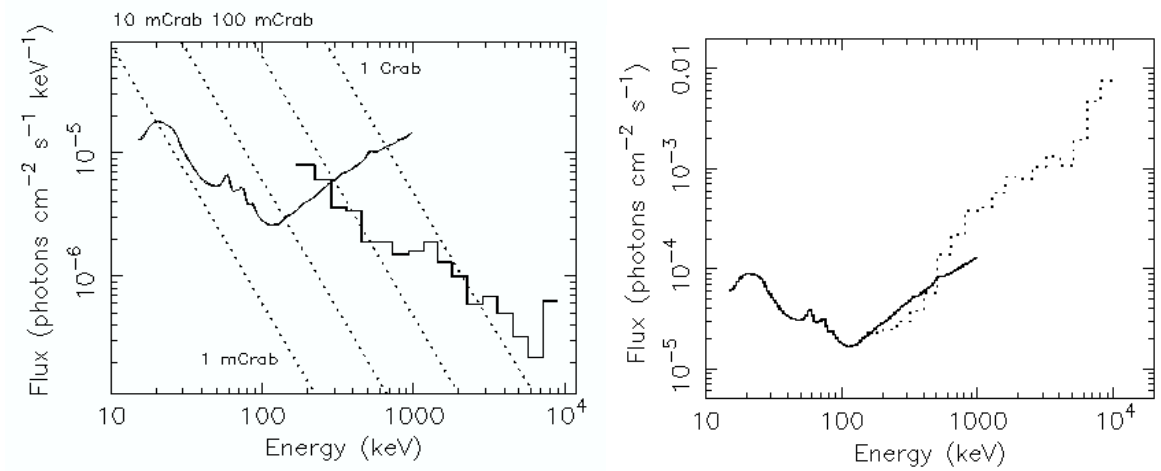

Figure 13. Overall IBIS 3σ continuum (left; 10^5 s) and narrow line (right; 10^5 s) sensitivity derived from empty field observations, and continuum binned to ΔE=E/2. Systematic errors (such as background uniformity) are not taken into account. ISGRI is from 15 to 1000 keV and PICsIT from 200 to 10^4 keV (single and multiple). Reference fluxes are for a power-law Γ=-2.

Table 4. ISGRI continuum sensitivities
(10^5 s exposure, 3σ detection, ΔE=E/2)

Energy (keV)	ph cm^{-2} s^{-1} keV^{-1}	Energy (keV)	ph cm^{-2} s^{-1} keV^{-1}	Energy (keV)	ph cm^{-2} s^{-1} keV^{-1}
15	12.8×10^{-6}	60	6.36×10^{-6}	300	6.02×10^{-6}
20	18.0×10^{-6}	70	5.02×10^{-6}	350	6.90×10^{-6}
25	16.0×10^{-6}	80	3.94×10^{-6}	400	7.56×10^{-6}
30	10.4×10^{-6}	90	3.46×10^{-6}	450	8.41×10^{-6}
35	7.54×10^{-6}	100	2.85×10^{-6}	500	9.83×10^{-6}
40	6.16×10^{-6}	150	3.12×10^{-6}	600	10.6×10^{-6}
45	5.59×10^{-6}	200	4.10×10^{-6}	700	11.6×10^{-6}
50	5.40×10^{-6}	250	5.03×10^{-6}	800	12.7×10^{-6}

Table 5. PICsIT continuum sensitivities
(10^5 s exposure, 3σ detection, ΔE=E/2; single and multiple events combined)

Start energy (keV)	End energy (keV)	ph cm^{-2} s^{-1} keV^{-1}	Start energy (keV)	End energy (keV)	ph cm^{-2} s^{-1} keV^{-1}
170	220	7.99×10^{-6}	1200	1400	1.88×10^{-6}
220	280	6.06×10^{-6}	1400	1800	1.28×10^{-6}
280	370	3.62×10^{-6}	1800	2200	1.05×10^{-6}
370	430	3.41×10^{-6}	2200	2900	0.59×10^{-6}
430	580	1.90×10^{-6}	2900	3500	0.68×10^{-6}
580	720	1.91×10^{-6}	3500	4500	0.50×10^{-6}
720	900	1.48×10^{-6}	4500	5700	0.32×10^{-6}
900	1200	1.57×10^{-6}	5700	7100	0.22×10^{-6}

Table 6. IBIS line sensitivities for a narrow (unresolved) line
(ISGRI and PICsIT, 10^6 s exposure, 3σ detection)

Energy (keV)	ISGRI line ph $cm^{-2}s^{-1}$	PICsIT line ph $cm^{-2}s^{-1}$	Energy (keV)	ISGRI line ph $cm^{-2}s^{-1}$	PICsIT line ph $cm^{-2}s^{-1}$
22.5	8.76×10^{-5}		566.1	8.40×10^{-5}	14×10^{-5}
28.4	6.28×10^{-5}		712.6	9.88×10^{-5}	22×10^{-5}
35.7	3.92×10^{-5}		897.2	11.9×10^{-5}	38×10^{-5}
45.0	3.13×10^{-5}		1129.5		$41x\ 10^{-5}$
56.6	3.71×10^{-5}		1421.9		57×10^{-5}
71.3	3.08×10^{-5}		1790.1		82×10^{-5}
89.7	2.17×10^{-5}		2253.6		79×10^{-5}
112.9	1.67×10^{-5}		2837.1		100×10^{-5}
142.2	1.98×10^{-5}		3571.7		$130x\ 10^{-5}$
179.0	2.54×10^{-5}	2.3×10^{-5}	4496.5		110×10^{-5}
225.4	3.21×10^{-5}	2.5×10^{-5}	5660.7		200×10^{-5}
283.7	4.27×10^{-5}	3.0×10^{-5}	7126.5		470×10^{-5}
357.2	5.31×10^{-5}	3.8×10^{-5}	8971.6		760×10^{-5}
449.6	6.64×10^{-5}	5.7×10^{-5}			

Table 7. ISGRI continuum sensitivities for an on-axis source

Energy band	Measured SNR (1)	Expected Crab flux (2) (ph cm^{-2} s^{-1})	Measured sensitivity (3) (ph cm^{-2} s^{-1})	Statistically limited sensitivity (AO5) (3) (ph cm^{-2} s^{-1})	Ratio (meas./AO5)
20-40 keV	1655	13.65×10^{-2}	13.45×10^{-6}	10.39×10^{-6}	1.3
40-100 keV	1006	7.36×10^{-2}	4.56×10^{-6}	5.02×10^{-6}	0.9
100-200 keV	272	2.22×10^{-2}	2.69×10^{-6}	3.12×10^{-6}	0.9

(1): Derived from Crab observations performed in Revolution 102 (see IBIS/ISGRI Validation Report V3.0, available at http://isdc.unige.ch?Support+documents).
(2): Using a power-law with photon index of 2.12 and a flux at 1 keV of 8 ph cm^{-2} s^{-1} keV^{-1}.
(3): Sensitivities for an exposure of 100 ks, $\Delta E=E/2$, 3σ at 30, 70 and 150 keV.

5.3.4 Off-axis instrument response

The off-axis response of the IBIS telescope has been characterized during the Crab calibration observations in 2004, 2005 and 2006. Note that the flux of off-axis sources can be reduced by up to 50% in the FOV at low energies (around 20 keV) with respect to OSA versions anterior to 4, as shown in Figure. This loss is linked to the mask supporting structure (including the nomex structure). The honeycomb structure of the nomex makes the absorption highly dependent on the angle as well as energy of incoming radiation (see Figure 17). Corrections to both images and spectra for off-axis sources are included in the OSA software versions 4 and higher, and these reduce any remaining off-axis effects to less than a few percent.

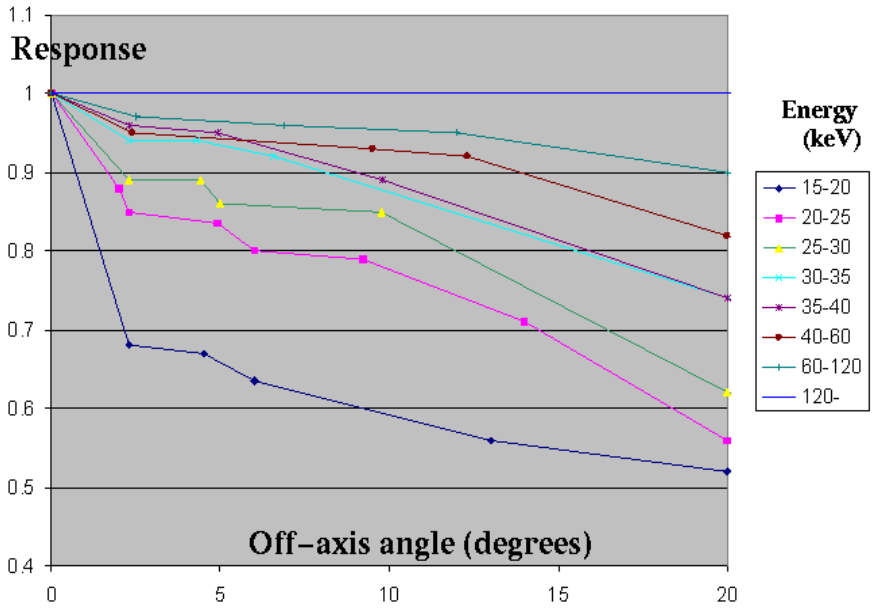

Figure 16. Deviations from the theoretical response (≡1) of the IBIS telescope for various off-axis angles in different energy bands. Note that the OSA software from version 4 onwards corrects for these deviations, see also Figure 17.

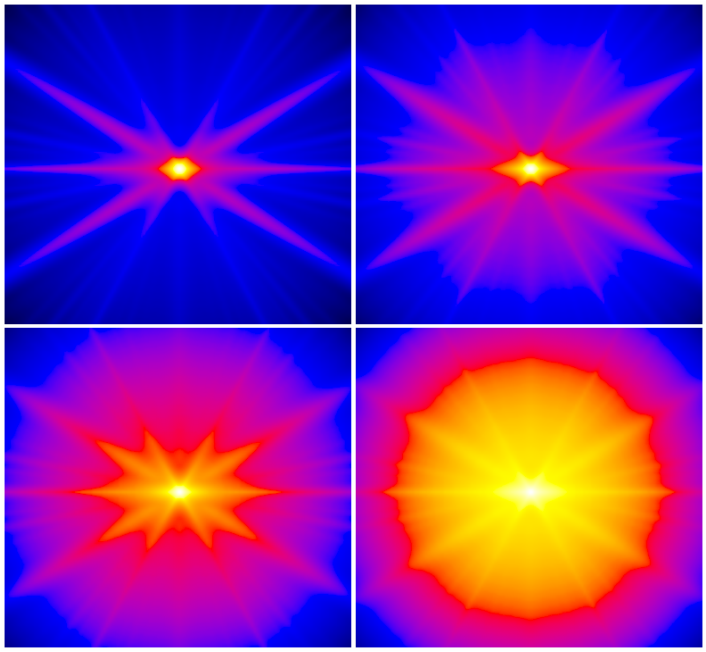

Figure 17. OSA 6.0 off-axis correction maps based on a detailed nomex geometrical model in the energy bands at 19.9-20.4 keV (top-left), 29.5-30.0 keV (top-right), 50-55 keV (bottom-left) and 250-300 keV (bottom-right). In these new maps, there is an important non-axisymmetric component characterized by the star-like shape which is due to the hexagonal honeycomb structure of the nomex.

5.3.5 Timing capabilities

The *time resolution* in ISGRI is 61.035 μs. For PICsIT, imaging and spectral histograms are collected every 1800-3600 seconds (depending on the flexible dithering time) - there is no finer time resolution available inside the histogram. The spectral timing data of PICsIT (no imaging!) will be accumulated every few ms; the resolution can be selected from ground and can take a value between 0.976 and 500 ms. The value used in routine operations is currently 15.625 ms. Once selected, it is applied to all PICsIT observations.

The *absolute timing accuracy,* i.e., the barycentric correction to event times measured in IBIS depends on the time resolution and on the time frame synchronisation in the instrument and spacecraft subsystems, and the uncertainty in the spacecraft position around the orbit. Calculations indicated a 1σ uncertainty of 61 μs and a 3σ uncertainty of 92 μs. Based on in-flight observations, the relative timing between the INTEGRAL instruments can be reconstructed within 10 μs, whereas the absolute timing accuracy is about 40 μs. A more accurate calibration might be performed via dedicated millisecond pulsar observations.

The dead-time in ISGRI is mainly due to encoding the events and to the coincidence applied with PICsIT, VETO and the calibration source. It amounts to about 24%. Variations are seen between the ISGRI modules and are linked to the count rates. For PICsIT the overall dead-time amounts to about 5-6%. Note that the PICsIT spectral timing channels are inverted in the pre-processing phase, and so in picsit_lcr.fits, extension numbers go from the highest to the lowest energy bin.

6 Observation "Cook book"

6.1 Astronomical considerations on the use of the instrument

In this section we present a summary of results obtained from observations with the IBIS instrument, illustrating its capabilities. The selection is by no means exhaustive.

From the second IBIS survey it is estimated that for a 1 Ms observation, a 1 mCrab source will be detected is a significance of 5σ in the energy range 20–100 keV, assuming negligible systematic errors as normally observed for extragalactic fields. This corresponds to a flux of $2x10^{-11}$ erg cm^{-2} s^{-1} in the 13–80 keV band.

In AO-1 and AO-2 most of the Core programme was devoted to the Galactic Center Deep Exposure (GCDE) and the Galactic Plane Scans (GPS). In AO-3 it was devoted to the Galactic Centre, Galactic latitude scans, Galactic arms (Scutum and Norma) and an extra-galactic field. In AO-4 and AO-5 the CP focused on deep observations of the Galactic plane, attempting to make the exposure as uniform as possible over the entire Galaxy by concentrating on underexposed regions. AO-6 is the last cycle during which CP observations will be perfoprmed; the time that remains amounts to 1.8 Ms and the ISWT has chosen to spend it observing the Perseus Arm. These will take place during the first 4 months of the observing cycle.

The third IBIS survey, using all CP and public data from launch to the end of April 2006 with a total exposure exceeding 40 Ms, revealed the presence of more than 400 sources detected in the 20-100 keV range down to ~1 mCrab. These included both transients and faint persistent objects. More than about 70% of the sky is covered by this survey with a minimum exposure of 10 ks. Of these sources, ~40% have been identified with Galactic accreting binary systems, ~30% with extra-galactic objects, and ~25% remain unknown in their nature. Thus far, IBIS has detected ~170 new objects[1]. The survey allowed us to determine that point sources account for most of the Milky Way's emission in hard X-rays/soft γ-rays in the range 20–300 keV, leaving at most a minor role for diffuse processes.

IBIS is able to detect any Galactic hard X/gamma–ray transient in outburst contained within its filed of view. Subsequent longer follow-up observations allow for the monitoring of the light curve of the transient, its spectral evolution, and possible transient lines with high spectroscopic quality. For example, the black-hole candidate transients IGR J17464-3213/H1743-322 and GX 339-4 have been monitored quite extensively, and state transitions have been seen. With regard to transient lines, the only example known is Nova Muscae 1991 (GS 1124-68), which showed a broad line at 480 keV—possibly redshifted annihilation—and another spectral feature near 200 keV, possibly due to Compton backscattering.

IBIS is also ideal to investigate whether black-hole binary systems are characterised by distinctive X/γ-ray signatures: are their spectra significantly harder than those from neutron-star systems? Is the bulk of their luminosity indeed in the soft γ-ray band? Can the spectral turn over

[1] A list of sources discovered by INTEGRAL ("IGR sources") is maintained by Jérôme Rodriguez, see http://isdc.unige.ch/~rodrigue/html/igrsources.html.

be measured and the total constrained? What is the nature of the high-energy excess seen in the spectra of known black hole candidates? Moreover, the good spectral resolution and large collecting area of IBIS allows for the study of cyclotron lines from magnetized NS in great detail through phase-resolved line shapes/widths.

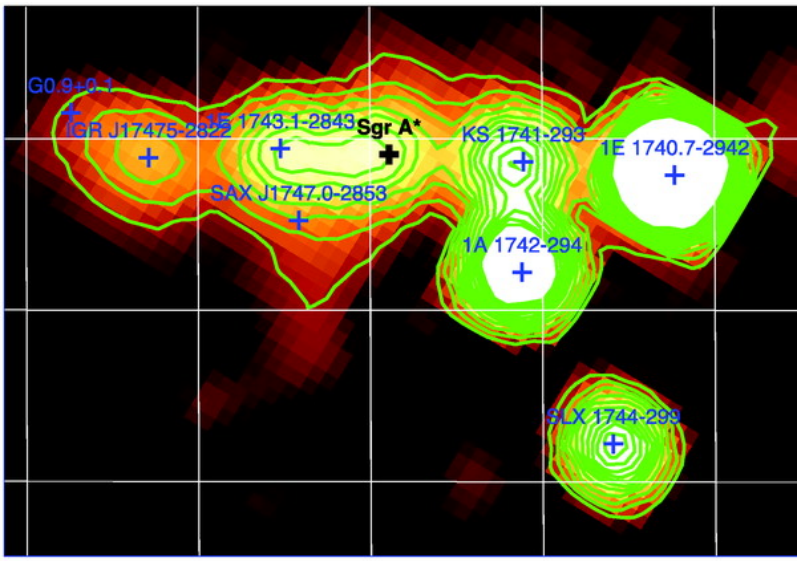

Figure 14. IBIS/ISGRI significance mosaic in the 20-40 keV band, using 7 Ms of data, with an effective exposure of 4.7 Ms at the position of Sgr A. The angular scale is about 2.5°x1.5°.*

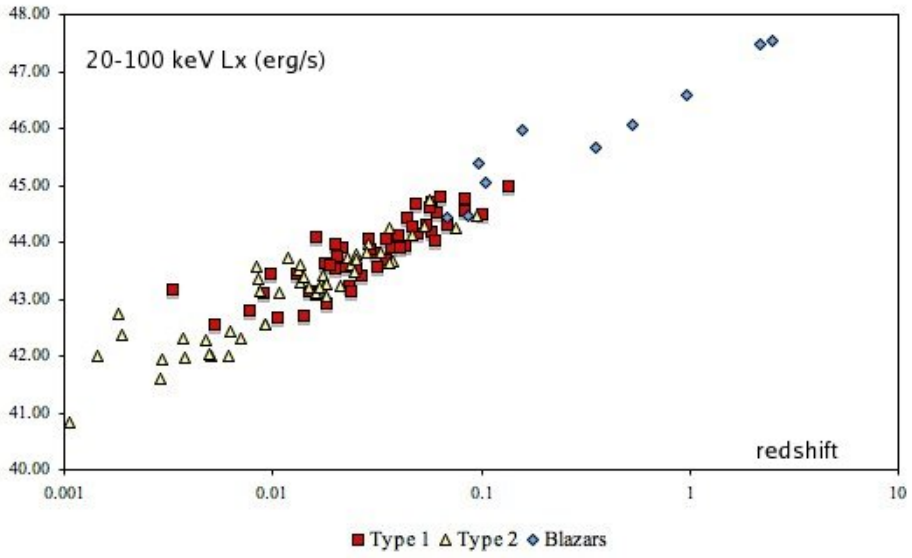

Figure 15. Luminosity (20-100 keV) versus redshift for AGN with known distance. The sample is taken from the third INTEGRAL/IBIS survey.

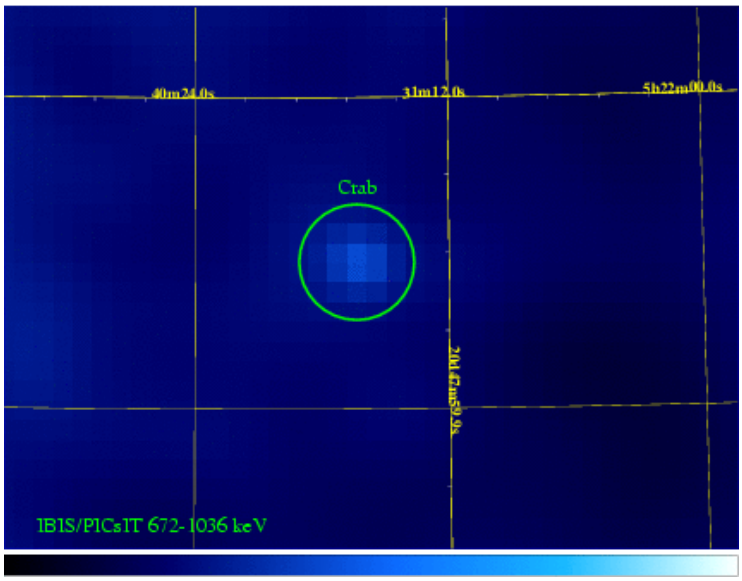

Figure 16. IBIS/PICsIT image of the Crab in the "MeV" range (672-1036 keV), using data based on 625 ks of net exposure time.

In the Galactic Centre region there are many highly variable sources in a small area of the sky, and is, therefore, subject to source confusion. However, thanks to the resolving power of IBIS and due to the variable nature of the sources, most of them can be studied individually on time scales of days. A rare type of γ-ray outburst 1 degree from the GC was detected on October 17, 2006, and a long follow-up observation campaign led the involved scientists to conclude that the source is most likely a new Black Hole : IGR J 17497-2821. The third IBIS survey catalog, with an exposure of ~5 Ms on the GC, reported the detection of 12 distinct sources in the central square degree (see also Figure 14).

With INTEGRAL one is able to study the statistics, demography and high-energy characteristics of nearby AGN. The third INTEGRAL/IBIS catalog contains around 130 sources detected in the 18–100 keV band that have been associated with active galaxies. This number is likely to increase as typically 20% of the unidentified IBIS sources are found to be associated with AGN of some type.

One of the most recent example is the identification of the source IGR J22517+2218 with the already known active galaxy MG3 J225155+2217, a quasar at z= 3.668. This makes it the most distant object detected by INTEGRAL so far. One more relevant example of the follow-up programmes is the identification of IGR J00234+6141, one of the faintest source discovered with IBIS, as a cataclysmic variable; these account for 5% of sources detected with IBIS. This is indicative that there are likely much more such faint system a significant fraction of the unresolved high energy background.

For those AGN with known distance, a plot of the 20-100 keV luminosity versus redshift (Figure 15), shows the range in parameters sampled by this survey and provides the sensitivity limit reached (~1.5×10^{-11} erg cm^{-2} s^{-1}). Most sources in the sample are Seyfert galaxies, almost equally divided between type 1 and 2 objects (with the interesting novelty of the first high-energy detections of 3 Narrow Line Seyfert 1); less than 10% are blazars and 22 are still

unclassified. Absorption is present in 53% of the objects with only around 10% of the total sample due to Compton-thick active galaxies. Note that since the third IBIS catalogue provides exposure and detection significance for each source detected, it can be also used by the interested observer to estimate the capability of INTEGRAL for specific extragalactic targets.

The MeV energy range is traditionally poor of sources, because of low fluxes and high background (see Table 3), and there is need for very long exposures to reach some detection. Nevertheless, IBIS can provide good sensitivity in this energy range useful for studies on bright Galactic compact objects (such as Cyg X-1 or the Crab, see, e.g., Figure 16). Moreover, IBIS provides also a very important instrument to study GRB in the MeV energy range with high time resolution (a few ms). In this energy range, the shielding is strongly reduced and the PICsIT detector acts as something like an "all-sky-monitor", with the possibility to detect GRB far away from the field of view.

Likely candidates of TeV sources have also been identified in the soft γ-ray and X-ray domain by using IBIS in conjunction with other instruments, thus opening a new window of scientific investigation. There are now 9 Pulsar Wind Nebulae identified at low energies (exclusing the Crab and Vela), all characterized by a soft γ-ray photon index of ~ 2.

6.2 How to calculate observing times

The approximate signal-to-noise ratio for a given exposure can be calculated from the sensitivity curves. As shown in *Eqs. 5.3.3.1* and *5.3.3.2*, the continuum sensitivity scales as $\Delta E^{-1/2}$, $t^{-1/2}$ and n_σ, and the line sensitivity as $t^{-1/2}$ and n_σ.

So, the signal-to-noise ratio achieved for a different time, t(s), ΔE/E and continuum or line flux Nc, Nl (photons cm^{-2} s^{-1} keV^{-1} and photons cm^{-2} s^{-1}, respectively), would be:

[Eq. 6.2.1.1] $n_\sigma = 3(N_c/S_c)(2\Delta E/E)^{1/2}\,(t/10^5)^{1/2}$ in the continuum, and

[Eq. 6.2.1.2] $n_\sigma = 3(N_l/S_l)\,(t/10^6)^{1/2}$ for a narrow (unresolved) line.

If the line is broad, with a FWHM of ΔE, then the signal-to-noise ratio is reduced by $(\Delta E/\delta E)^{1/2}$, where δE is the instrumental FWHM at that energy (see Figure 11 and Figure 12).

Note: for a 5x5 dither pattern a ~2% reduction in the signal-to-noise ratio compared to the above is to be taken into account. This does not apply to the hexagonal dither.

The results arising from the prescriptions given above should be treated as approximations only and be used as a *preliminary* feasibility check for a potential observation. We strongly recommend the *final* observation durations - those entered into the observing proposal - to be determined with the on-line Observation Time Estimator (OTE), accessible via the ISOC web site: http://integral.esa.int. The OTE will be used by ISOC to assess the technical feasibility of proposed observations, and advise the Time Allocation Committee (TAC) accordingly.

The continuum sensitivities (see Section 5.3.3) are given for ΔE = E/2 and can be extrapolated reliably to small energy ranges. However, when ΔE is greater than E/2, one in principle has to split the broad energy range into smaller energy bands, which all have individual ΔE smaller than E/2, then calculate the signal-to-noise or exposure times in each of these bands, and combine the results to get the appropriate values for the initial broad energy range. OTE takes care of this (unlike in AO1 and AO-2), by doing the split itself assuming a power-law spectrum

(where the observer is free to choose the value of the power-law index). The final OTE output is combined and presented into a single result. Currently, OTE provides support for power-law models only.

PLEASE NOTE: the continuum sensitivities shown in Section 5.3.3 and given are for ***mono-chromatic flux density (photons cm^{-2} s^{-1} keV^{-1})***, while the input for the OTE is in ***broad-band flux (photons cm^{-2} s^{-1})*** within a user-defined energy range.

6.3 Worked-out examples

Here we give some examples of how *Eqs. 6.2.1.1* and *6.2.1.2*, as well as OTE, can be used to assess the feasibility of "real|" observations.

6.3.1 Example 1

For a hard transient with a flux of 100 mCrab at 100 keV and a hard power law (photon spectral index Γ of -1) continuum above 100 keV, determine the achievable signal-to-noise ratio at 100 keV in an energy bin corresponding to the instrument FWHM at that energy.

Extrapolating the 2-10 keV flux of the Crab to the gamma-ray band, using a photon spectral index Γ of -2.1, a 100 mCrab source has a flux at 100 keV of

$N_c = 6.9 \times 10^{-5}$ photons cm^{-2} s^{-1} keV^{-1}.

At 100 keV only ISGRI is sensitive (it is below the energy range of PICsIT). The sensitivity curve (Figure 13 or Table 4) gives a flux sensitivity value at 100 keV of

$S_c = 2.85 \times 10^{-6}$ photons cm^{-2} s^{-1} keV^{-1}.

The energy resolution of ISGRI (FWHM, see Figure 11) at 100 keV is 8%;

$\Delta E/E = 0.08$.

Assume an observation time of 50 ks;

$t = 5 \times 10^4$ s.

This results in a signal-to-noise ratio (*Eq. 6.2.1.1*) of

$n_\sigma = 3 \times (6.9 \times 10^{-5} / 2.85 \times 10^{-6}) \times (2 \times 0.08)^{1/2} \times (5 \times 10^4 / 10^5)^{1/2} = 20.5\sigma$.

In comparison, the OTE indicates a 20σ detection for a 5x5 dither observation.

Note that OTE shows also that the source is easily detectable near 100 keV with ISGRI within 13 ks for a signal-to-noise ratio of 10σ.

6.3.2 Example 2

Consider the same source as in Example 1, but at higher energies, i.e., 800 keV.

Extrapolation of the 100 keV flux with the hard power law described above gives a 800 keV flux of

$N_c = 8.5 \times 10^{-6}$ photons cm^{-2} s^{-1} keV^{-1}.

PICsIT is more sensitive at 800 keV than ISGRI. The sensitivity curves (Figure 13 or Tables 4 and 5) indicate:

S_c (ISGRI) = 1.3 x 10^{-5} photons cm^{-2} s^{-1} keV^{-1},

S_c (PICsIT) = 1.5 x 10^{-6} photons cm^{-2} s^{-1} keV^{-1}.

The overall sensitivity compared to source flux is lower at 800 keV compared to 100 keV, so use a larger energy bin, e.g.,

$\Delta E/E = 0.15$.

Again assume a 50 ks observation;

$t = 5 \times 10^4$ s.

Perform the same calculation as in Example 1;

n_σ (ISGRI) = 0.8σ,

n_σ (PICsIT) = 6.6σ.

In comparison, the OTE gives 0.8σ and 6.4σ, respectively, for a 5x5 dither observation. So, the source will not be significantly detected by ISGRI within 50 ks.

OTE also shows that the source is detectable at 800 keV within 8.6 Ms and 123 ks, respectively with ISGRI and PICsIT, for a signal-to-noise ratio of 10σ.

6.3.3 Example 3

Consider the same transient as above but now, only the broad band flux is known.

The source flux in, for example, the 50-150 keV band is

$N_c = 7.6 \times 10^{-5}$ photons cm^{-2} s^{-1} keV^{-1}.

Assume again a 50 ks observation;

$t = 5 \times 10^4$ s.

Assuming a power-law spectrum (where we have input a photon spectral index of -1) OTE splits the 50-150 keV band into 3 smaller energy bands, i.e., 50-83 keV, 83-138 keV and 138-150 keV. In Table 8 we show the fluxes in these 3 bands as given by OTE, as well as the ISGRI sensitivities in these bands (see Figure 13 or Table 4), and calculate the significances using *Eq. 6.2.2.1 (*n_σ) and OTE (n_σ), assuming a 5x5 dither observation.

The calculated significances n_σ (4th column in Table 8) can be combined to determine the total significance in the 50-150 keV band:

$n_\sigma = 70\sigma$.

OTE combines the significances to a single value for the 50-150 keV band: 61σ (assuming a 5x5 dither observation). Compare this with the value one would get by directly using *Eq. 6.2.2.1* for the 50-150 keV range:

$n_\sigma = 3 \times (7.6 \times 10^{-5} / 2.85 \times 10^{-6}) \times (2 \times 100/100)^{1/2} \times (5 \times 10^4 / 10^5)^{1/2} = 80\sigma$,
i.e., one would be somewhat too optimistic in the latter case.

To detect the source with signal-to-noise ratio of 10σ in the 50-150 keV band one would need an exposure time of about 1.4 ks, as determined with OTE.

Table 8. OTE significance calculations for Example 3

Energy band (keV)	Flux (ph cm^{-2} s^{-1} keV^{-1})	Sensitivity (ph cm^{-2} s^{-1} keV^{-1})	n_σ	n_σ (OTE; 5x5 dither)
50-83	1.06×10^{-4}	5.0×10^{-6}	45	40
83-138	0.64×10^{-4}	2.6×10^{-6}	52	44
138-150	0.48×10^{-4}	3.0×10^{-6}	14	13

6.3.4 Example 4

Observations of a recent transient to search for the ^{22}Na line at 1.275 MeV (half life of 3.5 yr).

Assume that the model-predicted line flux after outburst is

$N_l = 1 \times 10^{-3}$ photons cm^{-2} s^{-1}.

The PICsIT line sensitivity curve (Figure 13 or Table 6) indicates

$S_l = 4.8 \times 10^{-4}$ photons cm^{-2} s^{-1}.

Assume a 500 ks observation;

$t = 5 \times 10^5$ s.

Then the line is detected at (*Eq. 6.2.1.2*):

$n_\sigma = 3 \times (1 \times 10^{-3} / 4.8 \times 10^{-4}) \times (5 \times 10^5 / 10^6)^{1/2} = 4.4\sigma$.

In comparison, the OTE indicates a 4.1σ detection for a 5x5 dither observation. To raise the detection significance to 10, the exposure time must be incrased to 3 Ms.